Full-sky maps for gravitational lensing of the cosmic microwave background

Carmelita Carbone,[1,2]★ Volker Springel,[3]★ Carlo Baccigalupi,[1]★ Matthias Bartelmann[4]★ and Sabino Matarrese[5]★

[1]*SISSA/ISAS, Astrophysics Sector, Via Beirut 4, I-34014, Trieste, Italy*
[2]*INFN, Sezione di Trieste, Via Valerio 2, 34127, Trieste, Italy*
[3]*Institut de Ciències de l'Espai, CSIC/IEEC, Campus UAB, F. de Ciències, Torre C5 par-2, Barcelona 08193, Spain*
[4]*Max-Planck-Institute for Astrophysics, Karl-Schwarzschild-Str. 1, D-85741 Garching, Germany*
[5]*Institut für Theoretische Astrophysik, Universität Heidelberg, Tiergartenstrasse 15, D-69121, Heidelberg, Germany*
[6]*Dipartimento di Fisica 'Galileo Galilei', Università di Padova, Padova, Italy*
[7]*INFN, Sezione di Padova, Via Marzolo 8, I-35131 Padova, Italy*

ABSTRACT

We use the large cosmological Millennium Simulation (MS) to construct the first all-sky maps of the lensing potential and the angle, aiming at gravitational lensing of the cosmic microwave background (CMB), with the goal of properly including small-scale non-linearities and non-Gaussianity. Exploiting the Born approximation, we implement a map-making procedure based on direct ray tracing through the gravitational potential of the MS. We stack the simulation box in redshift shells up to $z \sim 11$, producing continuous all-sky maps with arcmin angular resolution. A randomization scheme avoids the repetition of structures along the line of sight, and structures larger than the MS box size are added to supply the missing contribution of large-scale (LS) structures to the lensing signal. The angular power spectra of the projected lensing potential and the deflection-angle modulus agree quite well with semi-analytic estimates on scales down to a few arcmin, while we find a slight excess of power on small scales, which we interpret as being due to non-linear clustering in the MS. Our map-making procedure, combined with the LS adding technique, is ideally suited for studying lensing of CMB anisotropies, for analysing cross-correlations with foreground structures, or other secondary CMB anisotropies such as the Rees–Sciama effect.

Key words: gravitational lensing – cosmic microwave background.

1 INTRODUCTION

The cosmic microwave background (CMB) is characterized both by primary anisotropies, imprinted at the last scattering surface, and by secondary anisotropies caused along the way to us by density inhomogeneities and re-scatterings on electrons that are freed during the epoch of reionization, and heated to high temperature when massive structures virialize. One of the interesting effects that can generate secondary anisotropies is the weak gravitational lensing of the CMB, which arises from the distortions induced in the geodesics of CMB photons by gradients in the gravitational matter potential (Bartelmann & Schneider 2001; Lewis & Challinor 2006). Forthcoming, CMB probes do have the sensitivity and expected in-

strumental performance which may allow a detection of the lensing distortions of the primary CMB anisotropies, which would then also provide new insights and constraints on the expansion history of the Universe and on the process of cosmological structure formation (Acquaviva & Baccigalupi 2006; Hu, Huterer & Smith 2006). However, accurate predictions for the expected anisotropies in total intensity and polarization are clearly needed for analysing these future data, which demand detailed simulated maps.

The increasing availability of high-resolution *N*-body simulations in large periodic volumes makes it possible to directly simulate the CMB distortions caused by weak lensing using realistic cosmological structure formation calculations. This work represents a first step in that direction. Existing studies already give access to statistical properties of the expected all-sky CMB lensing signal, such as the two-point correlation function and the power spectrum of the lensing potential and deflection angle (see e.g. Lewis 2005 and references therein). This is based on 'semi-analytic' calculations that use approximate parametrizations of the non-linear evolution of the

★E-mail: carbone@ieec.uab.es (CC); volker@MPA-Garching.MPG.DE (VS); bacci@sissa.it (CB); mbartelmann@ita.uni-heidelberg.de (MB); sabino.matarrese@pd.infn.it (SM)

matter power spectrum. On the other hand, up to now *N*-body numerical simulations have been used to lens the CMB only on small patches of the sky in order to exploit the practicality of the flat-sky approximation (see e.g. Amblard, Vale & White 2004 and references therein). However, our approach of propagating rays through the forming dark matter structures gives access to the full statistics of the signal, including non-linear and non-Gaussian effects. Furthermore, it allows the accurate characterization of correlations of CMB lensing distortions with the cosmic large-scale (LS) structure, and with other foregrounds such as the Sunyaev–Zel'dovich (SZ) and Rees–Sciama effects. Hopefully, this will allow improvements in the methods for separating the different contributions to CMB anisotropies in the data, which would be of tremendous help to uncover all the cosmological information in the forthcoming observations.

From an experimental point of view, the improved precision of the CMB observations, in particular that of the next generation experiments,[1] may in fact require an accurate delensing methodology and a detailed lensing reconstruction. CMB experiments targeting, for instance, the CMB polarization, and in particular the curl component of the polarization tensor, the so-called *B* modes from cosmological gravitational waves, may greatly benefit from a precise knowledge of the lensing effects in order to separate them from the primordial cosmological signal (Seljak & Hirata 2004). In particular, for a correct interpretation of the data from the forthcoming *Planck* satellite,[2] it will be absolutely essential to understand and model the CMB lensing, as the satellite has the sensitivity and overall instrumental performance for measuring the CMB lensing with good accuracy. We note that the first detection of CMB lensing in data from the *Wilkinson Microwave Anisotropy Probe* (*WMAP*[3]) combined with complementary data has already been claimed by Smith, Zahn & Dore (2007) and Hirata et al. (2008).

In this study, we introduce a new methodology for the construction of all-sky lensing potential and deflection-angle maps, based on a very large cosmological simulation, the *Millennium* run (Springel, White & Hernquist 2005). As a first step in the analysis of the maps produced using the Millennium Simulation (MS) dark matter distribution, we have determined the interval of angular scales on which these maps match the semi-analytical expectations, since we expected a lack of lensing power on LSs, due to the finite volume of the *N*-body simulation. To compensate for this effect, we have implemented a method for adding LS power which allows to recover the correct lensing signal on the scales outside this interval, i.e. on scales larger than the MS box size. At the other extreme, at the smallest resolved scales, we are interested in the question whether our maps show evidence for extra lensing power due to the accurate representation of higher-order non-linear effects in our simulation methodology. On these small scales, the impact of non-Gaussianities from the mapping of non-linear lenses is expected to be largest.

This paper is organized as follows. In Section 2, we briefly describe the basic aspects of lensing relevant to our work. In Section 3, we describe the *N*-body simulation and the details of our map-making procedure. In Section 4, we present the lensing potential and deflection-angle maps, and study the distribution of power in the angular domain. In Section 5, we provide a summary and discussion.

2 LENSED MAPS OF THE CMB VIA THE BORN APPROXIMATION

In what follows, we will consider the *small-angle scattering* limit, i.e. the case where the *change* in the comoving separation of CMB light rays, owing to the deflection caused by gravitational lensing from matter inhomogeneities, is small compared to the comoving separation of the *undeflected* rays. In this case, it is sufficient to calculate all the relevant integrated quantities, i.e. the so-called *lensing potential* and its angular gradient, the *deflection angle*, along the undeflected rays. This small-angle scattering limit corresponds to the so-called 'Born approximation'.

We treat the CMB last scattering as an instantaneous process and neglect reionization. Adopting conformal time and comoving coordinates in a flat geometry (Ma & Bertschinger 1995), the integral for the projected lensing potential due to scalar perturbations with no anisotropic stress reads as

$$\Psi(\hat{n}) \equiv -2 \int_0^{r_*} \frac{r_* - r}{r_* r} \frac{\Phi(r\hat{n}; \eta_0 - r)}{c^2} \, \mathrm{d}r, \tag{1}$$

while the corresponding deflection-angle integral is

$$\boldsymbol{\alpha}(\hat{n}) \equiv -2 \int_0^{r_*} \frac{r_* - r}{r_* r} \nabla_{\hat{n}} \frac{\Phi(r\hat{n}; \eta_0 - r)}{c^2} \, \mathrm{d}r, \tag{2}$$

where r is the comoving distance, $r_* \simeq 10^4$ Mpc is its value at the last-scattering surface, η_0 is the present conformal time, Φ is the physical peculiar gravitational potential generated by density perturbations and $[1/r]\nabla_{\hat{n}}$ is the two-dimensional (2D) transverse derivative with respect to the line-of-sight pointing in the direction $\hat{n} \equiv (\vartheta, \varphi)$ (Hu 2000; Bartelmann & Schneider 2001; Refregier 2003; Lewis & Challinor 2006).

Actually, the lensing potential is formally divergent owing to the $1/r$ term near $r = 0$; nonetheless, this divergence affects the lensing potential monopole only, which can be set to zero, since it does not contribute to the deflection angle. In this way, the remaining multipoles take a finite value and the lensing potential field is well defined (Lewis & Challinor 2006). Analytically, the full information about the deflection angle is contained in the lensing potential, but numerically the two equations, (1) and (2), are generally not equivalent, and it will typically be more accurate to solve the integral (2) directly to obtain the deflection angle instead of finite differencing the lensing potential.

If the gravitational potential Φ is Gaussian, the lensing potential is Gaussian as well. However, the lensed CMB is non-Gaussian, as it is a second-order cosmological effect produced by cosmological perturbations on to CMB anisotropies, yielding a finite correlation between different scales and thus non-Gaussianity. This is expected to be most important on small scales, due to the non-linearity already present in the underlying properties of lenses.

The most advanced approach developed so far for the construction of all-sky lensed CMB maps (Lewis 2005) employs a semi-analytical modelling of the non-linear power spectrum (Smith et al. 2003), and derives from that the lensing potential and deflection-angle templates assuming Gaussianity. This approach is therefore accurate for what concerns the two-point correlation function of the lensing potential, as long as the non-linear two-point power of the matter is modelled correctly, but it ignores the influence of any statistics of higher order, which is expected to become relevant on small scales, where the non-linear power is most important. The use

---

of *N*-body simulations to calculate the lensing has the advantage of possessing a built-in capability of accurately taking into account *all* the effects of non-linear structure formation. On the other hand, the use of *N*-body simulations also faces limitations due to their limited mass and spatial resolution, and from their finite volume, as we will discuss later on in more detail.

For what concerns the line-of-sight integration in equations (1) and (2), the Born approximation along the *undeflected* photon path holds to good accuracy and allows to obtain results which include the non-linear physics. Even on small scales, in fact, this approximation can be exploited in the small-angle scattering limit, i.e. for typical deflections being of the order of arcmin or less (Hirata & Seljak 2003; Shapiro & Cooray 2006). For example, a single cluster typically gives deflection angles of a few arcmin, while smaller structures, such as galaxies, lead to arcsec deflections. Furthermore, it can be shown that the Born approximation also holds in 'strong' lensing cases, provided that the deflection angles are equally small. Finally, second-order corrections to the Born approximation (e.g. a non-vanishing curl component) are expected to be subdominant with respect to the non-linear structure evolution effects on small scales (Lewis & Challinor 2006). For these reasons, we argue that this approximation should be accurate enough for calculating all-sky weak lensing maps of the CMB based on cosmological *N*-body simulations.

3 MAP-MAKING PROCEDURE FOR THE MILLENNIUM SIMULATION

The MS is a high-resolution *N*-body simulation carried out by the Virgo Consortium (Springel et al. 2005). It uses $N = 2160^3 \simeq 1.0078 \times 10^{10}$ collisionless particles, with a mass of $8.6 \times 10^8 \, h^{-1} \, M_{\odot}$, to follow structure formation from redshift $z = 127$ to the present, in a cubic region $500 \, h^{-1}$ Mpc on a side, and with periodic boundary conditions. Here, h is the Hubble constant in units of $100 \, \text{km s}^{-1} \, \text{Mpc}^{-1}$. With 10 times as many particles as the previous largest computations of this kind (Colberg et al. 2000; Evrard et al. 2002; Wambsganss, Bode & Ostriker 2004), it features a substantially improved spatial and time resolution within a large cosmological volume.

The cosmological parameters of the MS are as follows. The ratio between the total matter density and the critical one is $\Omega_m = 0.25$, of which $\Omega_b = 0.045$ is in baryons, while the density of cold dark matter (CDM) is given by $\Omega_{CDM} = \Omega_m - \Omega_b$. The spatial curvature is assumed to be zero, with the remaining cosmological energy density made up by a cosmological constant, $\Omega_\Lambda = 0.75$. The Hubble constant is taken to be $H_0 = 73 \, \text{km s}^{-1} \, \text{Mpc}^{-1}$. The primordial power spectrum of density fluctuations in Fourier space is assumed to be a simple scale-invariant power law of wavenumber, with spectral index $n_s = 1$. Its normalization is set by the rms fluctuations in spheres of radius $8 \, h^{-1}$ Mpc, $\sigma_8 = 0.9$, in the linearly extrapolated density field at the present epoch. The adopted parameter values are consistent with a combined analysis of the 2dF Galaxy Redshift Survey (GRS) and the first year *WMAP* data (Colless et al. 2001; Spergel et al. 2003).

Thanks to its large dynamic range, the MS has been able to determine the non-linear matter power spectrum over a larger range of scales than possible in earlier works (Jenkins et al. 1998). Almost five orders of magnitude in wavenumber are covered (Springel et al. 2005). This is a very important feature for studies of CMB lensing, as we expect that this dynamic range, combined with the method for adding LS structures described in the next section, can be leveraged to obtain access to the full non-Gaussian statistics of

the lensing signal, limited only by the maximum angular resolution resulting from the gravitational softening length and particle number of MS. We stress again that the lensed CMB is non-Gaussian even if the underlying lenses do possess a Gaussian distribution. Moreover, the non-linear evolution of LS structures produces a degree of non-Gaussianity in the lens distribution which contributes to the non-Gaussian statistics of the lensed CMB on small scales. This non-Gaussian contribution can be computed only via the use of *N*-body simulations which are able to accurately describe the non-linear evolution of the lenses. These non-linearities are known to alter the lensed temperature power spectrum of CMB anisotropies by about ~ 0.2 per cent at $\ell \sim 2000$ and by ~ 1 per cent or more on smaller scales. But, much more notably, they introduce ~ 10 per cent corrections to the *B*-mode polarization power on *all the scales* (Lewis 2005; Lewis & Challinor 2006).

Our map-making procedure is based on ray tracing of the CMB photons in the Born approximation through the three-dimensional (3D) field of the peculiar gravitational potential. The latter is precomputed and stored for each of the MS output times on a Cartesian grid with a mesh of dimension 2560^3 that covers the comoving simulation box of volume $(500 \, h^{-1} \, \text{Mpc})^3$. The gravitational potential itself has been calculated by first assigning the particles to the mesh with the clouds-in-cells mass assignment scheme. The resulting density field has then been Fourier transformed, multiplied with Green's function of the Poisson equation in Fourier space, and then transformed back to obtain the potential. Also, a slight Gaussian smoothing on a scale r_s equal to 1.25 times the mesh size has been applied in Fourier space in order to eliminate residual anisotropies on the scale of the mesh, and a deconvolution to filter out the clouds-in-cells mass assignment kernel has been applied as well. The final potential field hence corresponds to the density field of the MS (which contains structures down to the gravitational softening length of $5 \, h^{-1}$ kpc) smoothed on a scale of $\simeq 200 \, h^{-1}$ kpc.

In order to produce mock maps that cover the past light cone over the full sky, we stack the peculiar gravitational potential grids around the observer (which is located at $z = 0$), producing a volume which is large enough to carry out the integration over all redshifts relevant for CMB lensing. For simplicity, we only integrate out to $z_* = 11.22$ in this study, which corresponds to a comoving distance of approximately $r_* \sim 7236 \, h^{-1}$ Mpc with the present choice of cosmological parameters. Indeed, the lensing power from still higher redshifts than this epoch is negligible for CMB lensing, as we will discuss in the next section. But, we note that our method could in principle be extended to still higher redshifts, up to the starting redshift $z = 127$ of the simulation.

The above implies that the simulation volume needs to be repeated roughly 14.5 times along both the positive and the negative directions of the three principal Cartesian axes *x*, *y* and *z*, with the origin at the observer. However, the spacing of the time outputs of the MS simulation is such that it corresponds to an average distance of $140 \, h^{-1}$ Mpc (comoving) on the past light cone. We fully exploit this time resolution and use 53 outputs of the simulation along our integration paths. In practice, this means that the data corresponding to a particular output time are utilized in a spherical shell of average thickness $140 \, h^{-1}$ Mpc around the observer.

The need to repeat the simulation volume due to its finite size immediately means that, without augmenting LS structures, the maps will suffer from a deficit of lensing power on large angular scales, due to the finite MS box size. More importantly, a scheme is required to avoid the repetition of the same structures along the line of sight. Previous studies that constructed simulated light-cone maps
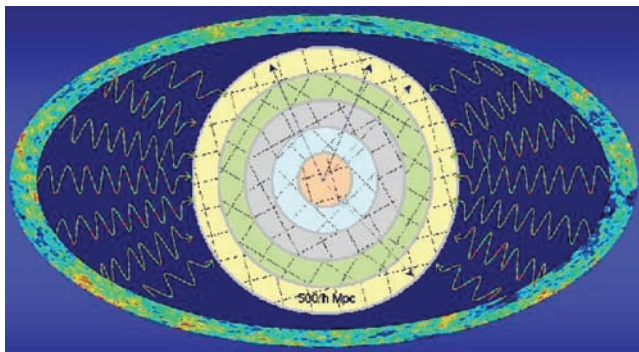
Figure 1. Sketch of the adopted stacking and randomization process. The passage of CMB photons through the dark matter distribution of the Universe is followed by stacking the gravitational potential boxes of the MS, which are $500\,h^{-1}$ Mpc on a side (comoving). Shells of thickness $500\,h^{-1}$ Mpc are filled with periodic replicas of the box. All boxes (squares) that fall into the same shell are randomized with the same coordinate transformation (rotation and translation), which, in turn, differs from shell to shell.

for small patches of the sky typically simply randomized each of the repeated boxes along the past light cone by applying independent random translations and reflections (e.g. Springel, Frenk & White 2001). However, in the present application this procedure would produce artefacts like ripples in the simulated deflection-angle field, because the gravitational field would become discontinuous at box boundaries, leading to jumps in the deflection angle. It is therefore mandatory that the simulated lensing potential of our all sky maps is everywhere continuous on the sky, which requires that the 3D tessellation of the peculiar gravitational potential is continuous transverse to every line of sight.

Our solution is to divide up the volume out to z_* into spherical shells, each of thickness $500\,h^{-1}$ Mpc comoving (obviously the innermost shell is actually a sphere of comoving radius $250\,h^{-1}$ Mpc, centred at the observer). All the simulation boxes falling into the

same shell are made to undergo the same, coherent randomization process, i.e. they are all translated and rotated with the same random vectors generating a homogeneous coordinate transformation throughout the shell. But, this randomization changes from shell to shell. Fig. 1 shows a schematic sketch of this stacking process. For simplicity, the diagram does not illustrate the additional shell structure stemming from the different output times of the simulation. As discussed before, this simply means that the underlying potential grid is updated on average three to four times with a different simulation output when integrating through one of the rotated and translated $500\,h^{-1}$ Mpc shells, but without changing the coordinate transformation. Note that our stacking procedure eliminates any preferred direction in the simulated all-sky maps.

In order to define the gravitational potential at each point along a ray in direction $\hat{\boldsymbol{n}}$, we employ spatial trilinear interpolation in the gravitational potential grid. It is then easy to numerically calculate the integral potential for each ray, based, for example, on a simple trapezoidal formula, which we use in this study. Obtaining the deflection angle could in principle be done by finite differencing a calculated lensing potential map, either in real space or in the harmonic domain. However, the accuracy of this approach would depend critically on the angular resolution of the map. Also, the sampling of the gravitational potential in the direction transverse to the line of sight varies greatly with the distance from the observer, so in order to extract the maximum information from the simulation data down to the smallest resolved scales in the potential field, we prefer to directly integrate up the deflection-angle vector along each light ray in our map. For this purpose, we first use a fourth-order finite-differencing scheme to compute the local 3D grid of the gradient of the gravitational potential, which is then again trilinearly interpolated to each integration point along a line of sight. In this way, we calculate the deflection angle directly via equation (2) along the paths of undeflected light rays.

Finally, we need to select a pixelization of the sky with a set of directions $\hat{\boldsymbol{n}} \equiv (\vartheta, \varphi)$. We here follow the standard approach introduced by the Hierarchical Equal Area Latitude Pixelization
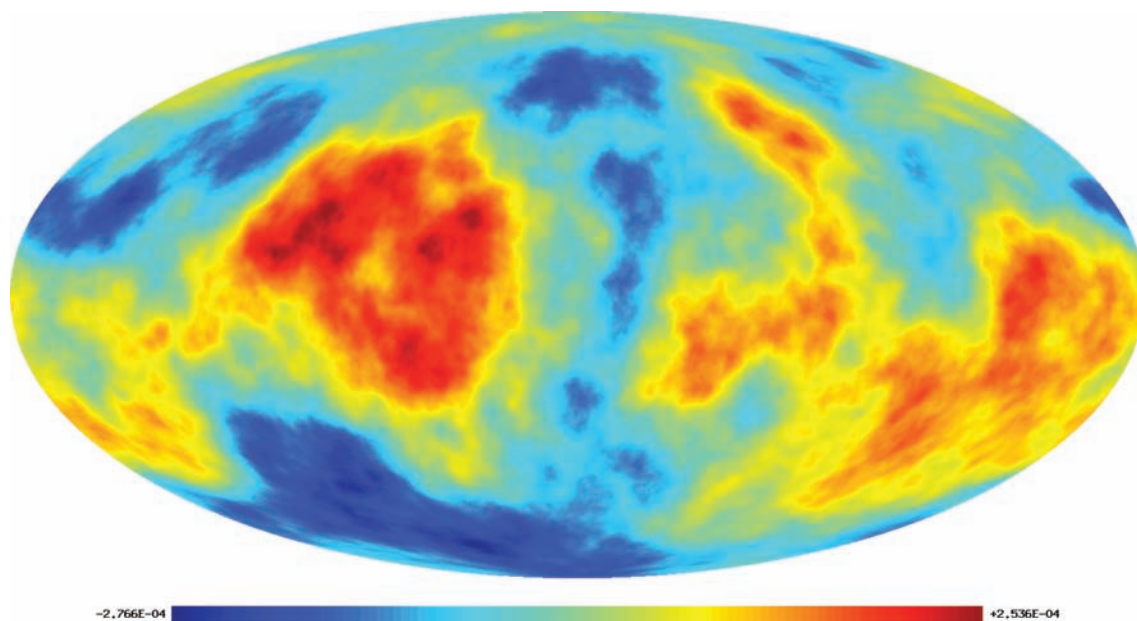
Figure 2. The simulated all-sky map of the lensing potential computed with the map-making procedure combined with the LS adding method as described in the text.
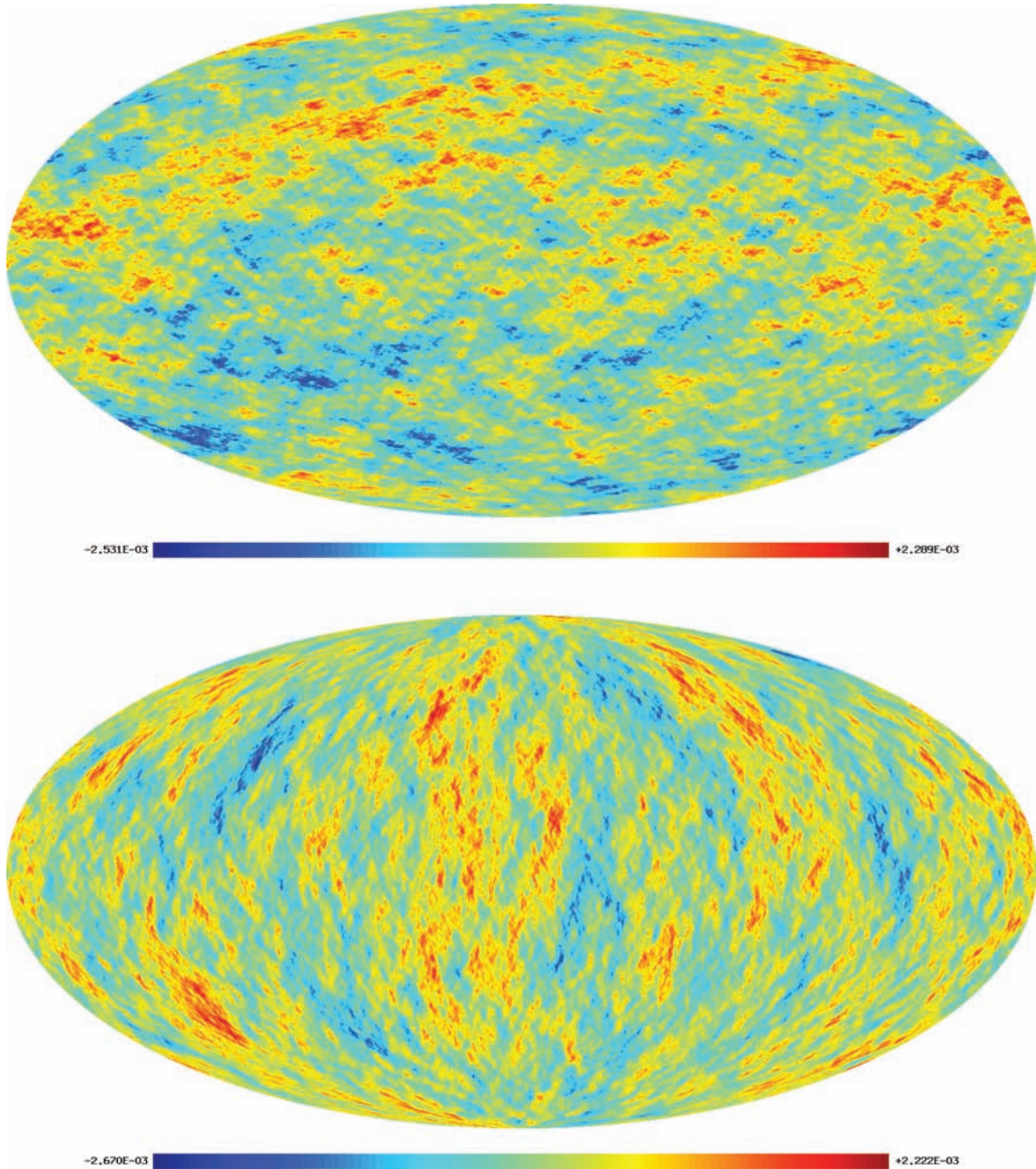
Figure 3. Simulated all-sky maps of the deflection-angle components along the ϑ direction (top panel), and along the φ direction (bottom panel), in radians.

(HEALPiX)[4] hierarchical tessellation of the unit sphere (Gorski et al. 2005).

4 SIMULATED MAPS OF THE LENSING POTENTIAL AND DEFLECTION ANGLE

In Figs 2–4, we show full-sky maps of the lensing potential, the deflection-angle ϑ/φ-components and the deflection-angle modulus $|\boldsymbol{\alpha}|$, respectively, obtained with the map-making technique described in the previous section combined with a semi-analytic procedure (to be explained below) augmenting the lensing power on scales beyond the MS box size. These maps are generated with a

[4] www.healpix.jpl.nasa.gov

HEALPiX pixelization parameter $N_{side} = 2048$, and have an angular resolution of $\sim$1.72 arcmin (Gorski et al. 2005), with 50 331 648 pixel in total.

Several interesting features should be noted in these maps. The distribution of the lensing potential, where the monopole and dipole have been cut to simplify the visual inspection, appears to be dominated by large features, which are probably simply arising from the projection of the largest scale gravitational potential fluctuations along the line of sight. However, the strength of local lensing distortions in the CMB cannot be directly inferred from the map of the lensing potential, as for the lensing deflection only the gradient of the potential is what really matters.

The maps showing the lensing deflection-angle components have interesting features as well. First of all, the signal in the two components of the deflection angle appears to possess two morphologically

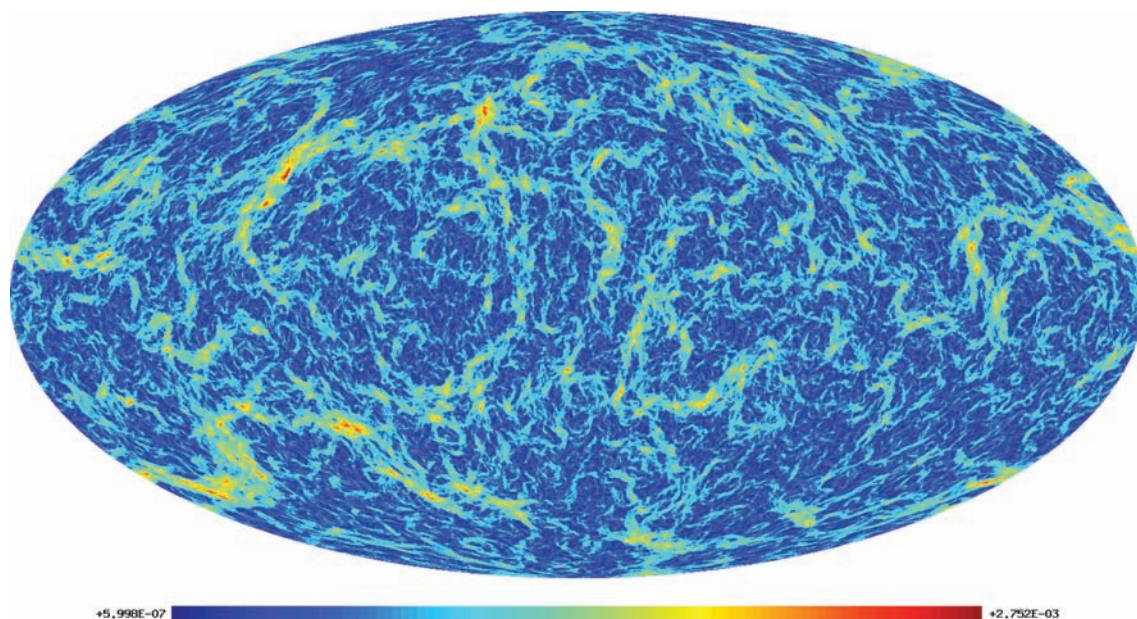+5.998E-07   +2.752E-03

Figure 4. Top panel: simulated all-sky map of the deflection-angle modulus (in radians), obtained with the map-making procedure combined with the LS adding method as described in the text.

distinct regimes, characterized on one hand by a diffuse background distribution, caused probably by the lines-of-sight where no dominant structures are encountered, and on the other hand by sharp features, caused probably by massive CDM structures which give rise to the largest deflections in the line-of-sight integration itself. The same features are evident in the map of the modulus of the deflection angle.

The mean value of $|\boldsymbol{\alpha}|$ in our simulated maps is 2.36 arcmin, while its standard deviation is 1.25 arcmin. The latter has to be compared with the corresponding value obtained via the angular differentiation of synthetic Gaussian maps produced with the lensing potential power spectrum generated by the publicly available Code for Anisotropies in the Microwave Background (CAMB[5]) using the MS cosmological parameters, as we explain in detail below. We find only a 0.03 per cent difference for the rms of the $|\boldsymbol{\alpha}|$-maps from MS and CAMB, when using the same maximum redshift of line-of-sight integration, i.e. $z_{max} = 11.22$. On the other hand, if we set $z_{max} = 1100$ in CAMB, we find that our estimate is $\sim$1.7 per cent smaller than the semi-analytic one, due to the missed contribution from sources beyond $z \sim 11$ in our map-making procedure. For comparison, we also evaluate semi-analytically the expected change in the standard deviation of $|\boldsymbol{\alpha}|$ when inserting in CAMB more recent estimates of the cosmological parameters (Komatsu et al. 2008). In this case, the rms from MS is $\sim$6 per cent and $\sim$4.2 per cent greater than the semi-analytical prediction when in CAMB we set $z_{max} = 11.22$ and 1100, respectively.

The lensing potential and deflection-angle maps of Figs 2 and 4 have been obtained combining the map-making procedure described in the previous section with the method for adding LS power that we now explain.

First, we have measured the power spectra of the simulated maps obtained from the MS scales only, i.e., using the routine ANAFAST of the HEALPix package, we have independently measured the power spectra of the lensing potential ($C_l^{\psi\psi}$) and deflection-angle modulus

($C_l^{\alpha\alpha}$) of the MS simulated maps, without exploiting the relations between the lensing potential and the ± 1-spin components of the deflection angle, which hold in the spherical harmonic domain (Hu 2000). Secondly, using the MS cosmological parameters, we have evaluated the semi-analytical power spectrum of the lensing potential from CAMB, including the estimate of the contribution from non-linearity (Smith et al. 2003) and stopping the line-of-sight integration redshift up to $z = 11.22$. Using the lensing potential power spectrum from CAMB, we have then produced the corresponding synthetic map (and its angular differentiation) obtained as a Gaussian realization generated with the HEALPix code SYNFAST, in order to produce the synthetic map of the deflection-angle modulus from the semi-analytic expectations of CAMB. From this map, we have then extracted the power spectrum of the deflection-angle modulus, and after deconvolution from the HEALPix pixel window function, we have compared it, together with the lensing potential power spectrum, to the corresponding deconvolved MS power spectra.

The top panel of Fig. 5 shows the primary result of this comparison. The black dash–dotted line represents the semi-analytic prediction of the lensing potential angular power spectrum obtained from CAMB as discussed above. This has been compared with the red dash–three-dotted line obtained with the map-making procedure previously described, which represents the result for the full integration starting at $z = 0$ and ending at $z = 11.22$. In this case, a power deficiency on LSs with respect to the semi-analytical prediction is evident, and confined to a multipole range corresponding to one degree or more in the sky. The same for the orange dotted line which gives the MS lensing potential power spectrum obtained from a line-of-sight integration starting at a redshift of $z = 0.22$ and ending at $z = 11.22$; comparing the two curves, a power decrease at low ℓ is easily observable in the orange dotted line, with respect to the red dash–three-dotted one, illustrating the influence of the lack of comoving scales greater than $500\,h^{-1}$ Mpc in the MS. As expected, this effect is evident in the multipole range corresponding to a few degrees or more, which is about the size of the MS box at the redshift most relevant for CMB lensing, i.e. $z \simeq 1$. However, towards larger ℓ, the deficit of LS power quickly decreases, and
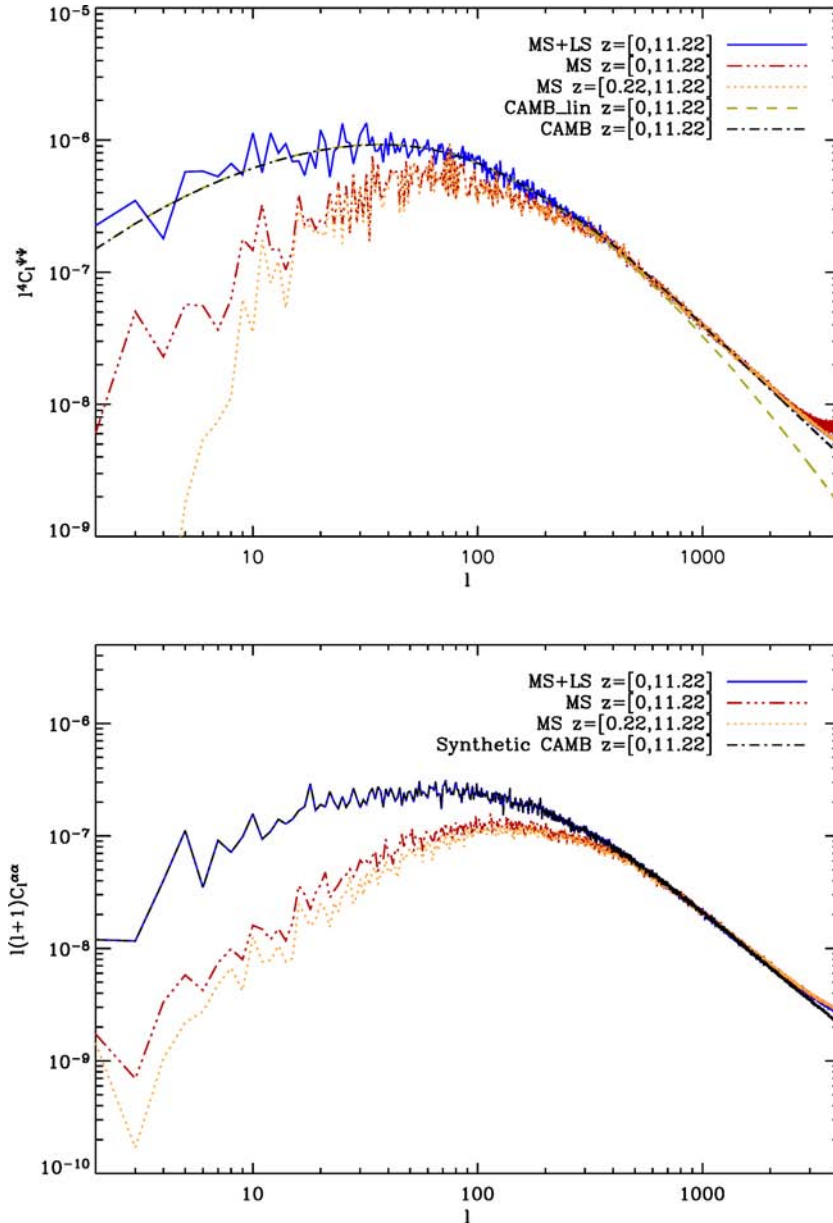
[5] See www.camb.info

Figure 5. Top panel: the power spectrum of the simulated lensing potential map of Fig. 2 (blue solid line), compared with the power spectrum of the lensing potential obtained with the CAMB code (dash–dotted black line), which also includes an estimate of the non-linear contributions (Smith et al. 2003). The red dash–three-dotted and orange dotted lines differ only in the starting redshift for the line-of-sight integration used in the map making. While the result shown in red begins at $z = 0$, the orange line gives the result for a start at $z = 0.22$. Finally, the light-green-dashed line represents the linear lensing potential power spectrum from the CAMB code. Bottom panel: the power spectrum (in radians squared) of the simulated deflection-angle modulus map shown in the upper panel of Fig. 4 (blue solid line), compared with the power spectrum (dash–dotted black line) of the synthetic deflection-angle modulus map obtained as a Gaussian realization from the CAMB lensing potential power spectrum. As above, the red dash–three-dotted and orange dotted lines differ only in the starting redshift of the line-of-sight integration, as labelled. The red line is for the full redshift interval and the orange one for a start at $z = 0.22$, as described in the text.

becomes negligible at scales $l \gtrsim 350$. Between these scales and $l \sim 2500$, there is quite good agreement between the MS lensing power spectrum and the semi-analytic prediction, but at $2500 \lesssim l \lesssim 4000$, the full MS signal for the lensing potential actually slightly exceeds the semi-analytic result. On this multipole range, the red dashed line is dominated by Poisson noise, but the slight excess of power is clearly observable from the orange dot line, in which there is no contribution from the low-redshift integration at $z \lesssim 0.2$. We ascribe this power excess to the matter non-linearities accurately reproduced from the MS. Finally, at $l \sim 4000$ the MS signal is

dominated by Poisson sampling noise from low-redshift potential integration. In fact, at very low redshifts, the 1.72 arcmin angular resolution of our map is comparable and even smaller than the intrinsic angular resolution corresponding to the spatial grid of the 3D gravitational potential field we use. This is evident in Fig. 6, where we compare the map angular resolution of 1.72 arcmin (red dashed line) with the effective angular resolution corresponding to the intrinsic grid spacing ($195\,h^{-1}$ kpc) of the 3D gravitational potential field as a function of redshift. Because the line-of-sight integral for the projected lensing potential involves a $1/r$ weighting term, the
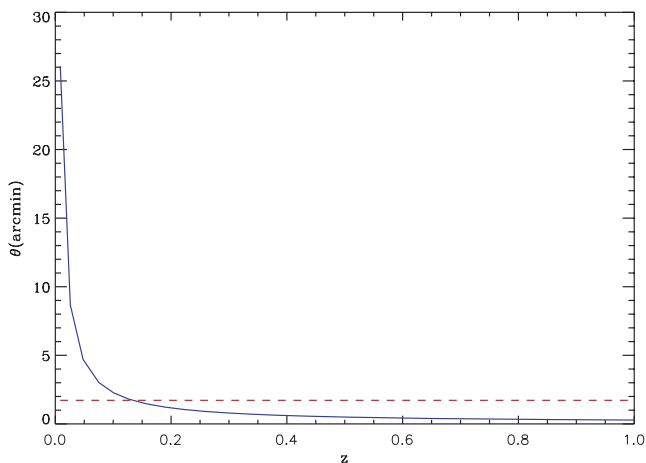
Figure 6. Comparison between the angular resolution of 1.72 arcmin of our full-sky maps (red dashed line) and the redshift-dependent, effective angular resolution (blue solid line) corresponding to the intrinsic grid spacing ($\sim 200\,h^{-1}$ kpc) of the 3D gravitational potential field constructed from the MS.

resulting noise terms are unfavourably amplified when the lensing potential is considered.

The above comparison has been used to evaluate the multipole range, $0 \lesssim l \lesssim 350$, not covered by the MS scales. On this interval we have applied the LS adding method: from the CAMB and MS maps of the lensing potential, we have extracted the two corresponding ensembles Ψ_{lm}^{CAMB} and Ψ_{lm}^{MS} of spherical harmonic coefficients, respectively. Since on low multipoles the effects of the non-Gaussianity from the non-linear scales are negligible and the Ψ_{lm} are independent, we have generated a joined ensemble of $\tilde{\Psi}_{lm}$, where $\tilde{\Psi}_{lm} = \Psi_{lm}^{CAMB}$ for $0 \leq l \leq 350$ and $\tilde{\Psi}_{lm} = \Psi_{lm}^{MS}$ for $l < 350$. Finally, we have generated the synthetic maps of the lensing potential and deflection angle as non-Gaussian constrained realizations, inserting the $\tilde{\Psi}_{lm}$ as input in SYNFAST, as shown in Figs 2–4.

These maps have the peculiarity of reproducing the non-linear and non-Gaussian effects of the MS non-linear dark matter distribution at multipoles $l < 350$, while at the same time including the contribution from the LSs at $l \leq 350$, where the lensing potential follows mostly the linear trend as shown from the light-green dot–dashed line in Fig. 5. The blue solid curve in the same figure represents the resulting power spectrum of the lensing potential map after the LS addition.

The bottom panel of Fig. 5 shows the corresponding power spectra for the physically and numerically more meaningful deflection angle. Here, we show a comparison of the power spectrum of the deflection-angle modulus ($C_l^{\alpha\alpha}$) measured for the MS simulated maps, in the absence of LS supplying, with the semi-analytic prediction constructed with CAMB and SYNFAST, as explained above. Again, we find a deficit of power on LSs, and a reassuring agreement over about one order of magnitude in l on intermediate scales. However, a slight excess of power over the semi-analytic predictions is easily seen at $l \gtrsim 2500$. As previously mentioned, it can be attributed to the non-linear evolution of the MS structures. Finally, the blue solid line represents the power spectrum extracted from the deflection-angle modulus map of Fig. 4, after adding LS structures.

Our map-making procedure offers very good resolution at the most important redshift for lensing of the CMB, $z \sim 1$ (see also Fig. 7), where the intrinsic angular resolution of our potential grid is six times better than the angular resolution of the full-sky map. We
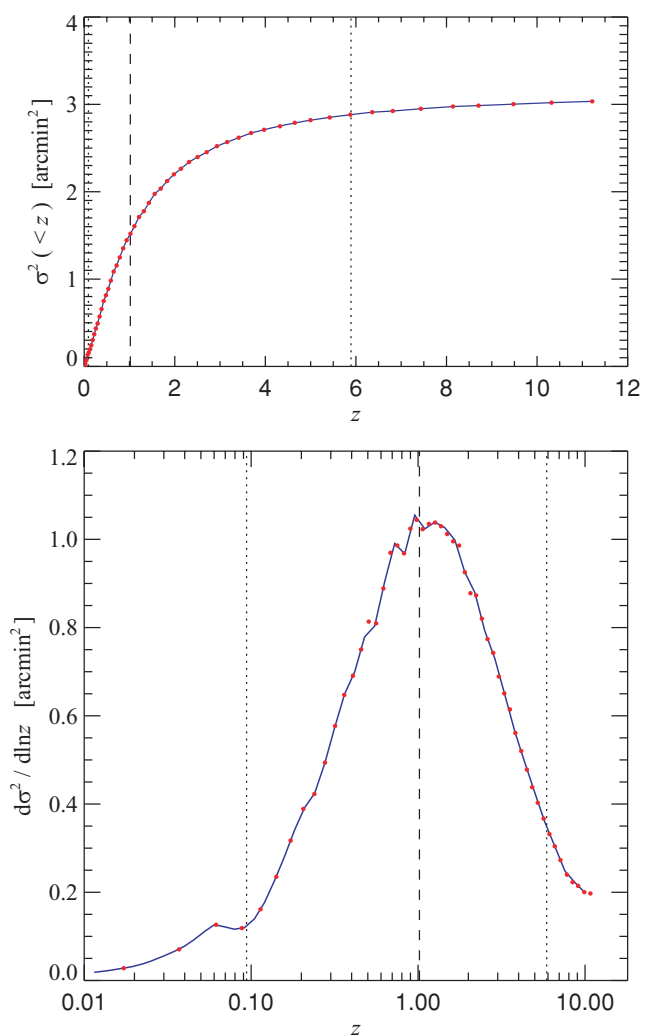

Figure 7. The cumulative and differential variance of the deflection-angle map as a function of redshift. The symbols mark the different output times of the MS. The vertical dashed line gives the redshift that corresponds to the 50 per cent quartile of the total variance in our maps, which is approximately at $z \sim 1$. The dotted lines mark the 5 and 95 per cent percentiles, indicating that 90 per cent of our signal in the deflection-angle power spectrum is produced in the redshift range $z \sim 0.1$ to ~ 6.0. Note, however, that we have lost a few per cent of the total power due to our truncation of the integration at $z = 11.22$. When included, this would slightly shift these percentiles to higher redshift.

therefore think that this higher small-scale power is a direct result of the more accurate representation of non-linear structure formation in our map simulation methodology. In fact, in our current maps we are still far from probing the most non-linear scales accessible in principle with our simulation. Those are a factor of 40 smaller (namely $5\,h^{-1}$ kpc) than resolved by the potential grid we have employed. However, using such a fine mesh is currently impractical, and would lead to angular resolutions in full-sky maps that are unaccessible even by the *Planck* satellite. However, for a smaller solid angle of the map, these scales can be probed with a different ray-tracing technique (Hilbert et al. 2007).

We note that the semi-analytic prediction for the power spectrum of the deflection-angle modulus has been evaluated as an angular gradient in the harmonic domain of a synthetic lensing potential Gaussian map; that is accurate since in this approach we work

with Fourier modes right from the start anyway. From a numerical point of view, the integral and derivative operators in equation (2) do, however, not commute, even if they analytically do, in the sense that finite differencing our measured projected potential will not necessarily give the same result as numerically integrating the deflection angle along each line of sight. The latter approach is more accurate, especially at a very high resolution, and it has been used by us in the comparison above since numerically integrating the deflection angle along each line of sight allows to preserve the contribution from the non-linear scales in a more efficient way than simply operating in the harmonic domain.

Finally, we consider the distribution of the deflection-angle power along the line of sight. In Fig. 7, we show the cumulative and differential variance of the deflection angle as a function of redshift. We see that the most important contributions to the final signal stem from $z \sim 1$, i.e. about half ways between the last scattering surface and the observer, as expected. This also allows us to assess the relative error introduced by stopping the integration at $z \simeq 11$, which is of the order of a few per cent, as mentioned above.

5 CONCLUSIONS

We constructed the first all-sky maps of the CMB weak-lensing potential and deflection angle based on a high-resolution cosmological *N*-body simulation, the Millennium Run Simulation. The lensing potential and deflection angle are evaluated in the Born approximation by directly ray tracing through a 3D, high-resolution mesh of the evolving peculiar gravitational potential and its gradient. The time evolution is approximated by 53 simulation outputs between redshift $z = 0$ and $z \simeq 11$, each used to cover a thin redshift interval corresponding to a shell in the past light cone around the observer. To prevent artificial repetition of structures along the line of sight, while at the same time avoiding discontinuities in the force transverse to a line of sight, we tessellate shells of comoving thickness corresponding to the size of the box ($500 \, h^{-1}$ Mpc) with periodic replicas which are coherently rotated and translated within each shell by a random amount. Moreover, in order to include the contribution to the lensing signal from the scales larger than the MS box size, we have implemented a method for adding LS structure as described in the text.

Using the HEALPix package for obtaining a uniform sky coverage, we have constructed simulated CMB lensing maps with nearly five million pixels and an angular resolution of $\sim$1.72 arcmin, based on potential fields calculated on 2560^3 meshes from the MS. In the present study, we analyse the power spectrum of the lensing potential and the deflection angle, and compare it with predictions made by semi-analytic approaches. We note that our general approach for map making can be extended to other CMB foregrounds, including the Integrated Sachs–Wolfe (ISW) and Rees–Sciama effects at low redshifts, as well as estimates of the SZ effects, or of the X-ray background. This will in particular allow studies of the cross-correlation of the lensing of CMB temperature and polarization with these effects, which will be the subject of a forthcoming study. In our approach, we do not take into account the contributions of the baryonic physics to the lensing effects on the CMB. We expect, in fact, that these contributions could be non-negligible only on the typical scales of cluster cores and below, thus well above $l \sim 3000$. Our comparison of the angular power spectrum of the Lensing potential and the deflection angle with semi-analytic expectations reveals two different regimes in our results. First, for multipoles up to

$l \sim 2500$, our simulated maps produce a lensing signal that matches the semi-analytic expectation. Second, we find evidence for a slight excess of power in our simulated maps on scales corresponding to a few arcmin and less, which we attribute to the accurate inclusion of non-linear power in the MS. It will be especially interesting to study the non-Gaussianities in the signal we found and its implied consequences for CMB observations.

The new method proposed here demonstrates that an all-sky mapping of CMB lensing can be obtained based on modern high-resolution *N*-body simulations. This opens a way towards a full and accurate characterization of CMB lensing statistics, which is unaccessible beyond the power spectrum with the existing semi-analytical techniques. This is relevant in view of the forthcoming CMB probes, both as a way to detect, extract and study the CMB lensing signal, which carries hints on the early structure formation as well as the onset of cosmic acceleration, and as a tool to distinguish CMB lensing from the Gaussian contribution due to primordial gravitational fluctuations.

REFERENCES

Acquaviva V., Baccigalupi C., 2006, Phys. Rev. D, 74, 103510
Amblard A., Vale C., White M., 2004, New Astron., 9, 687
Bartelmann M., Schneider P., 2001, Phys. Rep., 340, 291
Colberg J. M. et al., 2000, MNRAS, 319, 209
Colless M. et al., 2001, MNRAS, 328, 1039
Evrard A. E. et al., 2002, ApJ, 573, 7
Geller M. J., Huchra J. P., 1989, Sci, 246, 897
Gorski K. M. et al., 2005, ApJ, 622, 759
Gott J. R. I., Jurić M., Schlegel D., Hoyle F., Vogeley M., Tegmark M., Bahcall N., Brinkmann J., 2005, ApJ, 624, 463
Hilbert S., White S. D. M., Hartlap J., Schneider P., 2007, MNRAS, 382, 121
Hirata C. M., Seljak U., 2003, Phys. Rev. D, 68, 083002
Hirata C. M., Ho S., Padmanabhan N., Seljak U., Bahcall N., 2008, preprint (arXiv:0801.0644)
Hu W., 2000, Phys. Rev. D, 62, 043007
Hu W., Huterer D., Smith K. M., 2006, ApJ, 650, L13
Jenkins A. et al., 1998, ApJ, 499, 20
Komatsu E. et al., 2008, preprint (arXiv:0803.0547)
Lewis A., 2005, Phys. Rev. D, 71, 083008
Lewis A., Challinor A., 2006, Phys. Rep., 429, 1
Ma C. P., Bertschinger E., 1995, ApJ, 455, 7
Refregier A., 2003, ARA&A, 41, 645
Seljak U., Hirata C. M., 2004, Phys. Rev. D, 69, 043005
Shapiro C., Cooray A., 2006, JCAP, 0603, 007
Smith R. E. et al., 2003, MNRAS, 341, 1311
Smith K. M., Zahn O., Dore O., 2007, Phys. Rev. D, 76, 043510
Spergel D. N. et al., 2003, ApJS, 148, 175
Springel V., White M., Hernquist L., 2001, ApJ, 549, 681
Springel V., Frenk C. S., White S. D. M., 2006, Nat, 1137, 440
Wambsganss J., Bode P., Ostriker J. P., 2004, ApJ, 606, L93

This paper has been typeset from a TEX/LATEX file prepared by the author.